



# Effect of $\text{Al}_2\text{O}_3/\text{Na}_2\text{O}$ ratio and MnO on high-temperature properties of mold flux for casting peritectic steel

Le-jun Zhou<sup>1,2</sup> · Hao Luo<sup>1,2</sup> · Wan-lin Wang<sup>1,2</sup> · Xiong Yan<sup>1,2</sup> · Hou-fa Wu<sup>1,2</sup>

Received: 16 September 2021 / Revised: 16 November 2021 / Accepted: 17 November 2021 / Published online: 10 January 2022  
© China Iron and Steel Research Institute Group 2021

## Abstract

The influences of  $\text{Al}_2\text{O}_3/\text{Na}_2\text{O}$  ratio and MnO content on high-temperature properties, such as melting, crystallization, heat transfer, and viscosity of mold flux for casting peritectic steel, have been investigated. The results show that the melting temperatures of mold flux decrease, whereas the ratio of crystalline layers increases with the decrease in  $\text{Al}_2\text{O}_3/\text{Na}_2\text{O}$  ratio and increase in MnO content. The average response temperatures of the three mold fluxes decrease from 566, 525, to 512 °C, respectively, which indicates that the heat transfer controlling ability of mold flux is promoted due to the increase in crystallization ability and addition of transition metal oxide MnO. Furthermore, the viscosity–temperature curves suggest that the viscosity at 1300 °C decreases, but the break temperature increases with the reduction in  $\text{Al}_2\text{O}_3/\text{Na}_2\text{O}$  and addition of MnO.

**Keywords** Mold flux · Peritectic steel · Melting · Crystallization · Heat transfer · Viscosity

## 1 Introduction

Peritectic steels are crack-sensitive in the continuous casting process, since it undergoes a peritectic phase transition from  $\delta\text{-Fe}$  to  $\gamma\text{-Fe}$  ( $L + \delta\text{-Fe} \rightarrow \gamma\text{-Fe}$ ) during the solidification process [1, 2]. The mismatch on the thermal shrinkage coefficients of  $\delta\text{-Fe}$  and  $\gamma\text{-Fe}$  in peritectic steel causes additional stress on the initial solidified shell, and this stress may lead to the longitudinal cracks on the initial solidified shell [3, 4].

The usual strategy used to minimize longitudinal cracking is to uniformize the heat transfer and realize the moderate cooling at the initial solidification of the peritectic steel in casting mold. Mold flux with high crystallization ability is recognized as an effective way to reduce the heat flux from the molten steel to the mold wall [5–7]. The research from Cho and Shibata [8] suggested that the heat transfer ability of mold flux reduced with the increase

in basicity, since higher basicity enhanced the crystallization of mold flux. Similar results were also obtained by Wang et al. [9], Park and Sohn [10], and Susa et al. [11] who investigated the influences of  $\text{Na}_2\text{O}$ ,  $\text{Li}_2\text{O}$ , and  $\text{CaF}_2$  on the crystallization and heat transfer abilities of mold flux. In addition, mold flux containing transition metal oxides, such as MnO, FeO, and  $\text{TiO}_2$ , has additional impact on the heat flux across the mold flux film. The work from Diao et al. [12] showed that the heat flux was reduced with the addition of transition metal oxides, since the absorption coefficients and extinction coefficients of mold flux film increase rapidly with the addition of transition oxides.

Although lots of works related to the mold flux for peritectic steel have been carried out, most of them are focused on the crystallization behaviors. Very few of them considered comprehensively various properties of mold flux. Therefore, in this study, the effect of  $\text{Al}_2\text{O}_3/\text{Na}_2\text{O}$  ratio and MnO on some key high-temperature properties, such as melting, crystallization, heat transfer, and viscosity of peritectic steel mold flux, has been investigated.  $\text{Al}_2\text{O}_3$ ,  $\text{Na}_2\text{O}$ , and MnO were focused here since they are main components in mold flux, and the increase in  $\text{Na}_2\text{O}$  and MnO meanwhile decrease in  $\text{Al}_2\text{O}_3$  can enhance crystallization and reduce viscosity at the same time. These changes of properties of mold flux can improve its

✉ Wan-lin Wang  
wanlin.wang@gmail.com

<sup>1</sup> School of Metallurgy and Environment, Central South University, Changsha 410083, Hunan, China

<sup>2</sup> National Center for International Cooperation of Clean Metallurgy, Changsha 410083, Hunan, China

performance in the peritectic steel continuous casting process and consequently result in higher quality of casting product.

## 2 Experimental

### 2.1 Sample preparation

Mold flux samples, used in this study, were made from industrial raw materials, such as manganese carbonate, limestone, magnesia, wollastonite, bauxite, cement clinker, sodium carbonate, and fluorite. The major chemical compositions of these industrial raw materials were detected by induction coupled plasma-optical emission spectroscopy (ICP-OES; Spectro Blue Sop, Spectro, Germany), ion-selective electrode method (PF-2-01, Shanghai LEICI Corporation, China) and by X-ray fluorescence (XRF; S4 Pioneer, Bruker AXS, Karlsruhe, Germany). The analysis results are listed in Table 1.

The designed mold fluxes samples are based on a commercial mold flux for casting peritectic steel, and their chemical composition are listed in Table 2. These mold fluxes samples were prepared by mixing the industrial raw materials, firstly. Then, they were melted in an induction furnace at 1500 °C for 5 min to make sure that their compositions were homogeneous. After quenched in water, the glassy mold flux was dried and ground into powders for single/double hot thermocouple technique (SHTT/DHTT) and viscosity tests.

### 2.2 SHTT/DHTT tests

The melting, crystallization and heat transfer behaviors of mold fluxes were tested by SHTT and DHTT. The schematic of SHTT/DHTT apparatus is shown in Fig. 1 [13, 14]. There are two operation modes for the hot

thermocouple techniques. When one thermocouple is used, it is called SHTT; when the sample is loaded in-between the two B-type thermocouples, it is called DHTT.

The SHTT was adopted here for testing the melting behaviors of mold flux. The mold flux sample was firstly loaded on the B-type thermocouple (T.C.), and then it was continuously heated to 1500 °C at a heating rate of 10 °C/s as the stage I in Fig. 2. The change of the state of sample was observed and recorded by a charge-coupled device (CCD) camera which is connected to the optical microscope. Meanwhile, the temperature history of the sample was also recorded by the thermocouple simultaneously. The melting behavior of the mold flux could be studied based on the combination of in situ observation and real-time temperature.

The DHTT was used to study the crystallization ability of mold flux under the simulated temperature gradient, which is similar to that at the vicinity of meniscus in the casting mold. The temperature control profile of DHTT experiment is the stage II in Fig. 2. The mold flux sample, loaded in-between the two B-type thermocouples, was also heated to 1500 °C and maintained at that temperature for 3 min to eliminate bubbles and homogenize its chemical composition. The distance between the two thermocouples was 2 mm [15]. Then, one thermocouple named CH-1 was rapidly cooled from 1500 to 800 °C at a cooling rate of 30 °C/s; meanwhile, the other thermocouple named CH-2 was kept at 1500 °C. The temperatures of 1500 and 800 °C were chosen here since the former is close to that of solidified shell, while the latter is close to that of hot face of the solid slag film in the gap between mold wall and shell [16, 17].

The heat transfer of mold flux was tested immediately after the crystallization ability test. As illustrated in stage III in Fig. 2, the CH-1 was still maintained at 1500 °C, but the power of CH-2 was turned off. Under this situation, the thermocouple (CH-2) only worked as a temperature

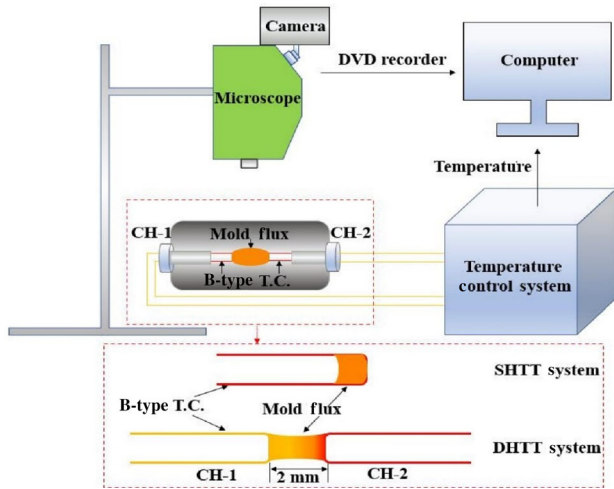
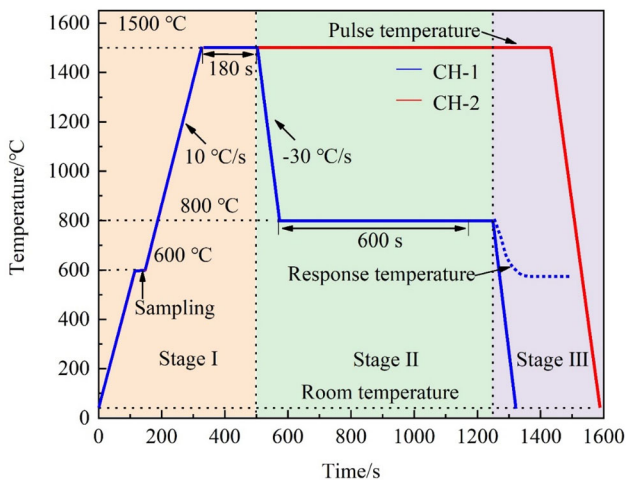
**Table 1** Composition of industrial raw materials (wt.%)

Raw material	CaO	SiO <sub>2</sub>	Al <sub>2</sub> O <sub>3</sub>	Na <sub>2</sub> O	MgO	CaF <sub>2</sub>	MnO
Manganese carbonate	0.96	–	0.04	0.21	0.10	–	60.33
Limestone	58.82	0.52	0.23	–	0.39	–	0.02
Magnesia	2.58	3.93	0.40	–	91.98	–	0.04
Wollastonite	47.49	51.06	0.08	–	0.95	–	0.05
Bauxite	0.54	22.33	61.41	0.13	0.37	–	0.01
Cement clinker	61.83	18.30	4.53	0.42	2.98	–	0.04
Sodium carbonate	0.01	–	–	58.38	0.00	–	–
Fluorite	–	3.64	0.24	0.00	0.25	94.56	0.02

**Table 2** Chemical composition of mold fluxes

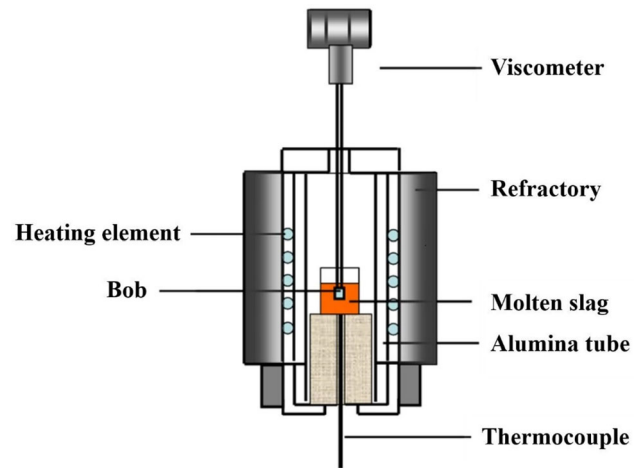
Mold flux	<i>R</i>	<i>A/N</i>	CaO/wt.%	SiO <sub>2</sub> /wt.%	Al <sub>2</sub> O <sub>3</sub> /wt.%	Na <sub>2</sub> O/wt.%	MgO/wt.%	F/wt.%	MnO/wt.%
Flux A	1.29	2.07	33.3	25.9	8.9	4.3	3.5	3.8	0.0
Flux B	1.29	1.44	33.3	25.9	7.2	5.0	3.5	3.8	1.0
Flux C	1.29	0.83	34.0	26.5	5.0	6.0	3.5	3.8	1.0

Basicity  $R = w_{\text{CaO}}/w_{\text{SiO}_2}$ ;  $A/N = w_{\text{Al}_2\text{O}_3}/w_{\text{Na}_2\text{O}}$ ;  $w_i$  content of component  $i$  in mold flux

**Fig. 1** Schematic diagram of SHTT/DHTT system [13, 14]**Fig. 2** Temperature control profiles of SHTT and DHTT test

detector. The temperature measured by CH-2 could be an important parameter to reflect the heat transfer ability of the mold flux in the mold.

After DHTT experiment, the samples were cooled down to room temperature, and then stripped from the thermocouples. The phase distribution in the mold flux after the DHTT experiment was analyzed by scanning electron

**Fig. 3** Schematic diagram of viscometer

microscopy (JSM-6360LV, Japanese Electronics Company, Japan).

### 2.3 Viscosity test

The viscosity test was carried out using the high-temperature rotary viscometer with a Brookfield viscometer (DV-II+, Brookfield Inc., USA). The schematic of the viscometer is shown in Fig. 3. A calibration measurement was carried out at room temperature around 25 °C through using castor oil with known viscosity of 0.28 Pa s [18–20]. When measuring the viscosity of those mold fluxes, first, about 150 g of sample powders were placed in a molybdenum crucible with the internal diameter, external diameter and height of 39, 49, and 80 mm, respectively. Then, the crucible was heated to 1310 °C and held for 10 min to obtain a homogeneous melt in an electric resistance furnace with MoSi<sub>2</sub> as heating element, under the protection from the pure argon gas. Then, the bob, which is also made of molybdenum with the height of 18 mm and the diameter of 15 mm, was immersed into the molten slag. Each measurement was performed during the cooling process, and the data of viscosity and temperature were collected every 5 s.

### 3 Results and discussion

#### 3.1 Melting behavior

The temperature history and snapshots of initial/complete melting of the three mold fluxes are shown in Fig. 4. A deviation was observed between the preset heating lines with the heat rate of 10 °C/s and the measured temperature history curves. This deviation was caused by the endothermic reaction of mold flux during the melting process. The temperature corresponding to the start point of the deviation is called the initial melting temperature ( $T_{\text{initial}}$ ), whereas the temperature corresponding to the end point of the deviation is called the complete melting temperature ( $T_{\text{complete}}$ ). At the initial melting temperature, most of the samples remained in powder state, and they turned into totally liquid at the complete melting temperature, as exhibited by these snapshots in Fig. 4.

Table 3 shows the initial and complete melting temperatures of the three mold fluxes. It can be seen that the initial temperatures of mold fluxes A, B, and C are 1218, 1186, and 1156 °C, whereas their complete melting temperatures are 1360, 1329, and 1314 °C. These suggest that the whole melting temperature range of mold flux decreases with the reduction in  $\text{Al}_2\text{O}_3/\text{Na}_2\text{O}$  ratio and increase in MnO content. The main reason is that  $\text{Na}_2\text{O}$  is a highly efficient fluxing agent, while  $\text{Al}_2\text{O}_3$  is a high-melting-point component. Thus, the addition of  $\text{Na}_2\text{O}$  and reduction of  $\text{Al}_2\text{O}_3$  can reduce the melting temperature of the mold fluxes greatly. In addition, MnO also has a possibility to work as fluxing agent in mold flux as previous studies [21, 22]; thus, the addition of MnO in the mold flux also helps to lower its melting temperature.

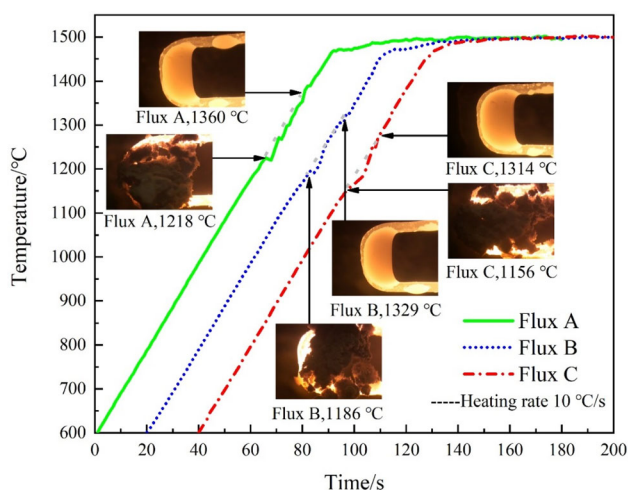


Fig. 4 Melting behaviors of mold fluxes

Table 3 Melting temperature range of mold fluxes (°C)

Mold flux	Flux A	Flux B	Flux C
$T_{\text{initial}}$	1218	1186	1156
$T_{\text{complete}}$	1360	1329	1314

#### 3.2 Crystallization behavior

Crystallization behavior of mold flux was investigated under the simulated temperature field. Figure 5 displays the two typical stages of mold flux A. Among them, Fig. 5a shows the state in which the flux is melted uniformly but has not yet begin to crystallize, and the temperatures of both CH-1 and CH-2 were 1500 °C at this time. Figure 5b shows the state of mold flux sample at the temperature gradient of 800 °C (CH-1)–1500 °C (CH-2). Generally, the slag film in-between the two thermocouples is composed of glassy layer, crystalline layer and liquid layer. However, those layers cannot be distinguished clearly since the glassy and liquid layers are not transparent. This opacity results from the industrial raw materials, which contain some colorant impurities.

In order to investigate the morphologies and distributions of the precipitated phases in mold fluxes, the mold fluxes after the DHTT test were analyzed by scanning electron microscopy and are shown in Figs. 6–8. Among them, Figs. 6a, 7a and 8a are the overall view of the samples after the DHTT tests; Figs. 6b–d, 7b–d and 8b–d are the magnified zones at the interface of liquid/crystalline layers, crystalline/glassy layers and crystalline layer; Figs. 6e–g, 7e–g and 8e–g are the further magnified images at those zones for observing the morphologies of precipitated crystalline phases.

From Figs. 6a, 7a and 8a, it can be seen that the obvious three-layer structure appears on the mold fluxes. They are the liquid layer close to the high-temperature CH-2, glassy layer close to the low-temperature CH-1, and the crystalline layer in the middle. Generally, the morphologies of crystals close to the glassy layer and liquid layer are different. The crystals close to the lower temperature glassy layer are more likely to be dendritic, while those close to the higher temperature liquid layer are more bulk. In addition, the size of crystals close to the glassy layer are smaller than those close to the liquid layer. The main reason for that is the different kinetic conditions for the crystallization at the lower and higher temperature regions close to liquid layer should be more relaxed, and there are more spaces for the migration of ionic clusters.

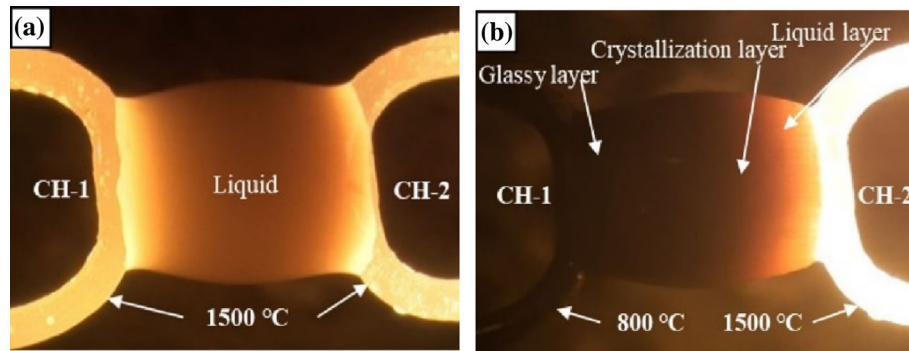


Fig. 5 Crystallization behaviors of mold flux under simulated thermal gradient. **a** Before crystallization; **b** after crystallization

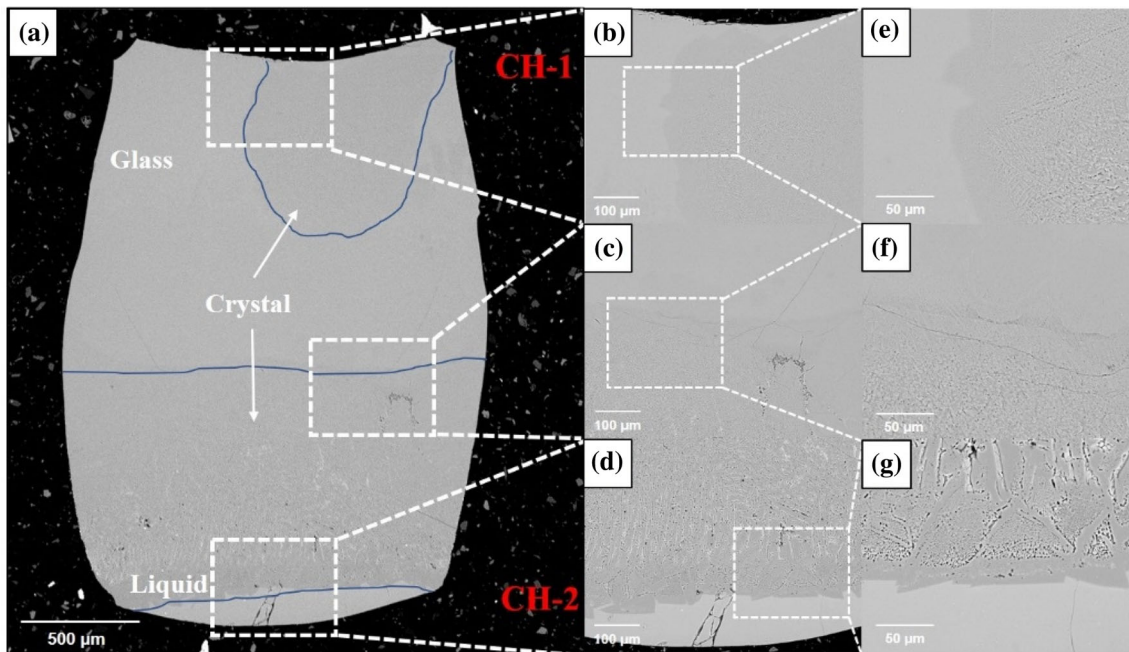


Fig. 6 Scanning electron microscopy (SEM) images of mold flux A

Those are beneficial for the crystallization, which resulted in the larger bulk crystals at the higher temperatures regions.

The ratios of the liquid, crystalline, and glassy layers of mold fluxes at the final steady state after the DHTT tests were obtained using the Image J software, and the results are listed in Table 4. The ratio of liquid layer in the three mold fluxes A, B and C increases from 3.9% to 5.3%, and to 9.3%. This variation trend is consistent with the change of the melting temperature range as shown in Table 3. In addition, the ratio of crystalline layer increases from 60.3% to 75.8% with the decrease in Al<sub>2</sub>O<sub>3</sub>/Na<sub>2</sub>O ratio and increase in MnO content in mold fluxes A–C. The reduction of Al<sub>2</sub>O<sub>3</sub> in mold flux can enhance the crystallization since it works as network former in basic melt system [23]. In addition, the increase in Na<sub>2</sub>O and MnO contents in mold flux (Table 1) can also promote the crystallization of

mold flux, since the free oxygen O<sup>2-</sup> provided by them can depolymerize the melt structure, which is beneficial for the transfer of clusters [24, 25].

### 3.3 Heat transfer

The heat transfer ability of mold flux in this study was characterized by the measured temperatures from the free low-temperature CH-1 of DHTT as shown in stage III in Fig. 2. Figure 9 shows the temperature history of CH-1 after it was power off. The average response temperatures of the free CH-1 in the three mold fluxes A, B, and C are 566, 525, and 512 °C, respectively. The mold flux C shows the best heat transfer controlling ability which is needed for the moderate cooling of peritectic steel since its measured temperature is the lowest, and that ability of flux B and flux C is relatively weaker.

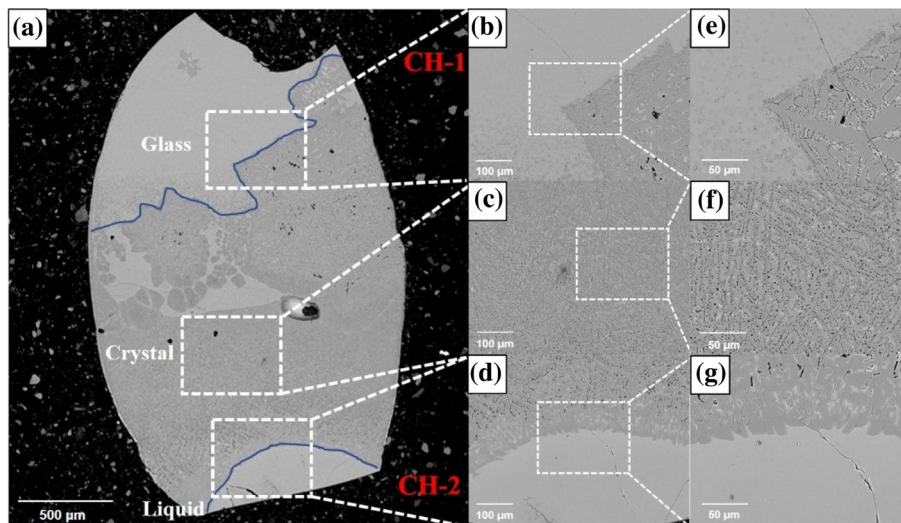


Fig. 7 SEM images of mold flux B

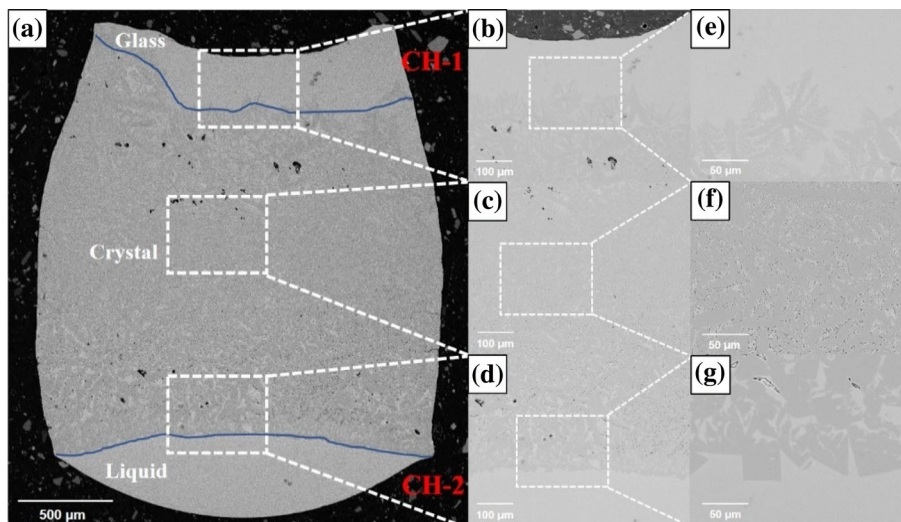


Fig. 8 SEM images of mold flux C

**Table 4** Ratio of different layers in mold fluxes (%)

Mold flux	Glassy layer	Crystalline layer	Liquid layer
Flux A	35.9	60.3	3.9
Flux B	28.6	66.2	5.3
Flux C	14.9	75.8	9.3

In fact, the heat transfer ability of mold flux is mainly determined by two factors. One is the ratios of the liquid, crystalline and glassy layers, since liquid layer has the highest heat transfer coefficient, glassy layer ranks second, and the crystalline layer owns the lowest [26, 27]. The other is the containing of transition metal oxides which

have a significant effect on absorption coefficients and extinction coefficients of mold fluxes [12, 28, 29]. The addition of transition metal oxides, such as MnO, FeO, and TiO<sub>2</sub>, will block the heat transfer, especially the radiation heat flux, which will weaken the heat transfer ability of mold flux. Therefore, the ratio of crystalline layer in flux C is the highest as listed in Table 4, and the addition of 1 wt. % MnO can also help to block the heat transfer from the high-temperature CH-2 to the free low-temperature CH-1, resulting in the lowest response temperature.

### 3.4 Viscosity

The viscosity–temperature curves of the three mold fluxes are shown in Fig. 10. There are two typical parameters, the

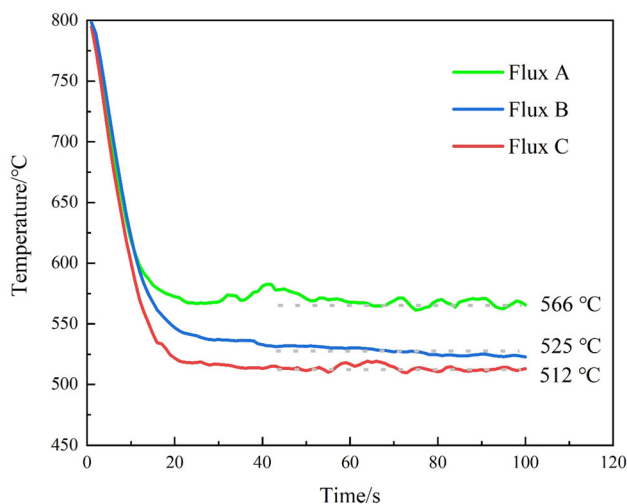


**Fig. 9** Heat transfer curve of mold fluxes

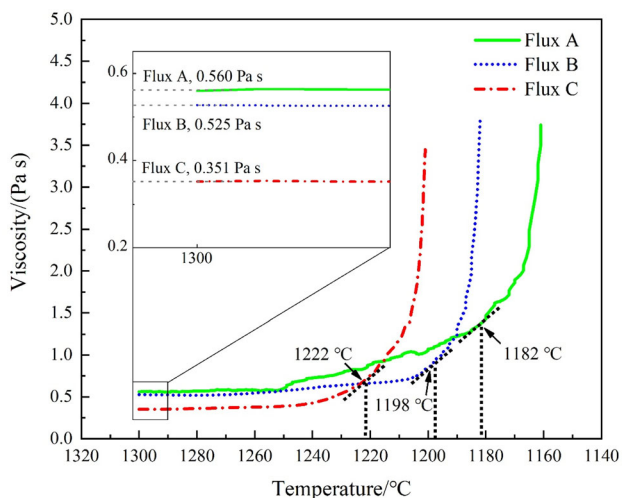


**Fig. 10** Viscosity-temperature curves of mold fluxes

viscosity at 1300 °C and break temperature, which can represent the rheological performance of mold flux. 1300 °C is the average temperature of liquid mold flux on the top of molten steel in the casting mold, while break temperature is the temperature at which the mold flux starts to lose its flowability [30–32]. The viscosity at 1300 °C and break temperature of these mold fluxes obtained from Fig. 10 are shown in Table 5.

**Table 5** Viscosity at 1300 °C and break temperature of mold fluxes

Mold flux	A	B	C
Viscosity/(Pa s)	0.560	0.525	0.351
Break temperature/°C	1182	1198	1222

From Fig. 10, it can be known that the viscosity increases with the decrease in temperature, especially at the low-temperature region. The viscosity increases rapidly, when the temperature drops below the break temperature. It is attributed to that the distance between ionic clusters in molten slag gets shorter, especially when temperature drops lower than break temperature. Thus, the resistance for the migration of ionic clusters increases, leading to the increase in viscosity.

Furthermore, it can be found from Fig. 10 and Table 5 that the viscosity at 1300 °C decreases from 0.560 Pa s (mold flux A) to 0.525 Pa s (mold flux B) and to 0.351 Pa s (mold flux C) with the decrease in Al<sub>2</sub>O<sub>3</sub>/Na<sub>2</sub>O and addition of MnO. It is reasonable since the increase in Na<sub>2</sub>O and MnO can provide more O<sup>2-</sup> to break the Si–O–Si into Si–O<sup>-</sup>, which depolymerizes the melt structure. Moreover, the reduction of Al<sub>2</sub>O<sub>3</sub> content can also simplify the melt structure and reduce the viscosity since the network former from Al<sub>2</sub>O<sub>3</sub> decreases. Contrary to the variation of viscosity at 1300 °C, the break temperature of the mold flux increases from 1182 (mold flux A), 1198 (mold flux B) and 1222 °C (mold flux C), which is consistent with crystallization ability of mold flux. In fact, for high basicity slag, the break temperature is mostly determined by the precipitation of crystals in melt. The mold flux C owns the highest crystallization ability; thus, its break temperature is also the highest.

## 4 Conclusions

1. The initial temperatures of mold fluxes A, B, and C are 1218, 1186, and 1156 °C, whereas their complete melting temperatures are 1360, 1329, and 1314 °C. These suggest that the whole melting temperature range of mold flux decreases with the reduction in Al<sub>2</sub>O<sub>3</sub>/Na<sub>2</sub>O ratio and increase in MnO content.
2. There is an obvious three-layer structure on the mold fluxes samples, and the ratio of crystalline layer increases from 60.3% to 75.8% with the decrease in Al<sub>2</sub>O<sub>3</sub>/Na<sub>2</sub>O ratio and increase in MnO content in mold fluxes A–C.
3. The average response temperatures of the free CH-1 in the three mold fluxes A, B and C decrease from 566 to 525 and to 512 °C, respectively, which indicates that the heat transfer controlling ability of mold flux is promoted due to the increase in crystallization ability and addition of transition metal oxide MnO.
4. The viscosity at 1300 °C decreases from 0.560 (mold flux A) to 0.525 (mold flux B) and to 0.351 Pa s (mold flux C) with the decrease in Al<sub>2</sub>O<sub>3</sub>/Na<sub>2</sub>O and addition of MnO. However, the break temperature of the mold flux increases from 1182 (mold flux A), 1198 (mold

flux B) and 1222 °C (mold flux C), which is consistent with crystallization ability of mold flux.

**Acknowledgements** This work was supported by the National Natural Science Foundation of China (Grant Nos. 51874363 and U1760202), Natural Science Foundation of Hunan Province (Grant No. 2019JJ40345), and Hunan Scientific Technology Projects (Grant Nos. 2020WK2003 and 2019RS3007).

## References

- [1] S. Griesser, C. Bernhard, R. Dippenaar, *Acta Mater.* 81 (2014) 111–120.
- [2] D.P. Li, H.W. Wu, H.F. Wang, H. Li, *J. Iron Steel Res. Int.* 27 (2020) 782–787.
- [3] W.L. Wang, X. Yan, L.J. Zhou, S.L. Xie, D.Y. Huang, *Metall. Mater. Trans. B* 47 (2016) 963–973.
- [4] Y.H. Sun, Y.J. Ni, Z.B. Xu, K.K. Cai, C.M. Chang, M.S. Ma, X. Du, X.R. Jin, *J. Iron Steel Res. Int.* 15 (2008) No. S1, 165–175.
- [5] L.J. Zhou, W.L. Wang, F.J. Ma, J. Li, J. Wei, H. Matsuura, F. Tsukihashi, *Metall. Mater. Trans. B* 43 (2012) 354–362.
- [6] L.J. Zhou, W.L. Wang, K.C. Zhou, *ISIJ Int.* 55 (2015) 1916–1924.
- [7] L.J. Zhou, W.L. Wang, B.X. Lu, G.H. Wen, *Met. Mater. Int.* 21 (2015) 126–133.
- [8] J.W. Cho, H. Shibata, *J. Non-Cryst. Solids* 282 (2001) 110–117.
- [9] H. Wang, P. Tang, G.H. Wen, X. Yu, *Ironmak. Steelmak.* 38 (2011) 369–373.
- [10] J.Y. Park, I. Sohn, *Int. J. Heat Mass Transf.* 109 (2017) 1014–1025.
- [11] M. Susa, Y. Kono, R. Endo, Y. Kobayashi, *Adv. Molten Slags, Fluxes and Salts* 1 (2016) 327–334.
- [12] J. Diao, B. Xie, J.P. Xiao, C.Q. Ji, *ISIJ Int.* 49 (2009) 1710–1714.
- [13] L.J. Zhou, W.L. Wang, D.Y. Huang, J. Wei, J. Li, *Metall. Mater. Trans. B* 43 (2012) 925–936.
- [14] W.L. Wang, P.S. Lyu, L.J. Zhou, H. Li, T.S. Zhang, *JOM* 70 (2018) 1248–1255.
- [15] K.C. Mills, A.B. Fox, Z. Li, *Ironmak. Steelmak.* 32 (2005) 26–34.
- [16] L.J. Zhou, W.L. Wang, R. Liu, B.G. Thomas, *Metall. Mater. Trans. B* 44 (2013) 1264–1279.
- [17] J. Yang, Y. Cui, L. Wang, Y. Sasaki, J. Zhang, O. Ostrovski, Y. Kashiwaya, *Steel Res. Int.* 86 (2015) 636–643.
- [18] L.J. Zhou, W.L. Wang, *Metall. Mater. Trans. B* 47 (2016) 1548–1552.
- [19] W.L. Wang, S.F. Dai, L.J. Zhou, J.K. Zhang, W.G. Tian, J.L. Xu, *Ceram. Int.* 46 (2020) 3631–3636.
- [20] L.J. Zhou, W.L. Wang, *Metall. Mater. Trans. B* 48 (2017) 220–226.
- [21] C.L. Chen, L. Zhang, W. Steven, S.Y. Sun, J. Sharif, H. Tom, J. Iron Steel Res. Int. 16 (2009) No. S2-2, 1116–1120.
- [22] S.J. Zhang, W.H. Ma, P. Zhang, J.H. Wen, S.L. Liu, *Metall. Res. Technol.* 116 (2019) 317.
- [23] J.Y. Chen, W.L. Wang, L.J. Zhou, Z.H. Pan, *J. Iron Steel Res. Int.* 28 (2021) 552–562.
- [24] W.L. Wang, H.Q. Shao, L.J. Zhou, H. Luo, H.F. Wu, *Ceram. Int.* 46 (2020) 26880–26887.
- [25] J. Kim, I. Sohn, *J. Non-Cryst. Solids* 379 (2013) 235–243.
- [26] L.J. Zhou, W.L. Wang, J. Wei, M.Y. Jin, *ISIJ Int.* 53 (2013) 665–672.
- [27] D.T. Stone, B.G. Thomas, *Can. Metall. Quart.* 38 (1999) 363–375.
- [28] X. Qiu, B. Xie, X.M. Qing, J. Diao, Q.Y. Huang, S.B. Wang, *J. Iron Steel Res. Int.* 20 (2013) No. 11, 27–32.
- [29] Q.F. Shu, Q.Q. Li, T. Fabritius, *Metals* 9 (2019) 516.
- [30] L.J. Zhou, H. Li, W.L. Wang, I. Sohn, *Steel Res. Int.* 88 (2017) 1600459.
- [31] K.C. Mills, A.B. Fox, *ISIJ Int.* 43 (2003) 1479–1486.
- [32] S. Sridhar, K.C. Mills, O.D.C. Afrange, H.P. Lörz, R. Carli, *Ironmak. Steelmak.* 27 (2000) 238–242.